PNAS RESEARCH ARTICLE | BIOPHYSICS AND COMPUTATIONAL BIOLOGY

Theory of chromosome structural dynamics by processive loop extrusion

Zhiyu Cao[a,1], Chaoqun Du[b,1], Zhonghuai Hou[b,2], and Peter G. Wolynes[a,c,d,2]

Affiliations are included on p. 8.

Contributed by Peter G. Wolynes; received March 18, 2026; accepted April 25, 2026; reviewed by Masaki Sasai and Bin Zhang

The processivity of Structural Maintenance of Chromosome complexes defines the characteristic run length and lifetime of loop extrusion events, which set up the large-scale architecture of chromosomes. We introduce an active, non-Markovian mechanistic model that explicitly incorporates motor processivity to provide a statistical mechanical treatment that identifies the nontrivial effects induced by the processive character of such active motors. At low activity, in interphase, processive loop extrusion generates effective cooperative multibody interactions, which lead to the so-called "chromatin jets." Upon increasing activity, symmetry breaking occurs, as seen in the characteristic, cylindrically anisotropic mitotic chromosome organization. The strength of the motor processivity determines whether the symmetry breaking transition leads to crystalline ordering or to liquid-crystalline architectures for the mitotic chromosome.

active matter | loop extrusion | motor proteins | polymer physics

Significance

Structural maintenance of chromosomes complexes such as cohesin and condensin actively organize genomes by extruding DNA loops. A key property of these motors is their processivity–the distance and duration over which loop extrusion persists. Understanding how this parameter influences large-scale chromosome architecture is essential. Here we develop a statistical mechanical framework to describe processive loop extrusion and show that motor activity generates effective many-body interactions that reorganize chromatin over long genomic distances. Our results reveal how nonequilibrium loop extrusion can produce distinct collective chromosome architectures called "jets," which have recently been observed.

The spatial organization of chromosomes represents a challenge for nonequilibrium statistical physics. In interphase, chromatin forms a hierarchy of globally disordered loops and domains (1), whereas during mitosis, the chromosome becomes compact and forms an ordered, rod-like structure, proving that the isotropic symmetry is broken (2). Accumulating experimental and theoretical evidence indicates that the transition between these architectures is dynamically shaped by Structural Maintenance of Chromosome (SMC) complexes, such as cohesin and condensin, which actively extrude DNA loops in an ATP-dependent manner (3–12). These motors are notoriously susceptible to the forces they are called upon to exert (3, 13, 14). A key kinetic parameter controlling the activity of SMC complexes is their processivity–the distance, speed, and time over which a motor can extrude DNA before dissociating from it. Single-molecule and in vivo imaging experiments have revealed that processivity varies widely across cell types and between SMC forms (3, 14–17). While cohesin displays only limited processivity during interphase, condensin II can extrude hundreds of kilobases during mitosis (3, 13, 18). Previous theoretical models have successfully explored various aspects of active loop extrusion kinetics or chromatin folding (19–22), but we believe a theoretical framework explicitly treating the coupling between motor processivity and chromatin dynamics is needed, owing to the susceptibility of SMC motors.

In our recent works, we demonstrated that the effective energy landscape, fractal-globule scaling, and the symmetry-breaking mitotic phase can all emerge from a Markovian "grappling motor" model, as revealed through a combination of variational analysis and stochastic simulations (23–25). In this paper, we develop a nonequilibrium mechanistic model that explicitly incorporates SMC motor processivity along with the coupling of motor activity to chromatin dynamics. In addition to the polymer chain coordinates, accounting for occupancy variation allows the formulation of a full kinetic many-body Master equation. By projecting out the motor occupancy degrees of freedom, we can then derive an effective statistical–mechanical energy landscape theory that identifies the nontrivial effects that are induced by active, processive motors. Our analysis shows that loop extrusion not only generates pair interactions like those inferred from Hi-C measurements that lead to an "ideal chromosome" (26–28), but also generates effective cooperative multibody interactions whose range and symmetry depend on the extrusion processivity. These emergent interactions lead to distinctive chromosomal structural patterns known as chromatin jets, which have been observed in the Hi-C experiments (29). We further predict that varying motor processivity can systematically transform the mitotic chromatin first from a crystalline state to a soft-crystalline state and finally to a liquid-crystalline state as processivity increases.

Author contributions: Z.C. and P.G.W. designed research; Z.C., C.D., Z.H., and P.G.W. performed research; Z.C. and P.G.W. contributed new reagents/analytic tools; Z.C., C.D., and Z.H. analyzed data; and Z.C. and P.G.W. wrote the paper.

Reviewers: M.S., Kyoto Daigaku; and B.Z., Massachusetts Institute of Technology.

The authors declare no competing interest.

Copyright © 2026 the Author(s). Published by PNAS. This article is distributed under Creative Commons Attribution-NonCommercial-NoDerivatives License 4.0 (CC BY-NC-ND).

[1]Z.C. and C.D. contributed equally to this work.

[2]To whom correspondence may be addressed. Email: hzhlj@ustc.edu.cn or pwolynes@rice.edu.

This article contains supporting information online at https://www.pnas.org/lookup/suppl/doi:10.1073/pnas.2609796123/-/DCSupplemental.

Published May 28, 2026.

Downloaded from https://www.pnas.org by CAS University of Science and Technology of China USTC on May 29, 2026 from IP address 218.22.21.23.

Model

We construct a model that simultaneously accounts for both chromatin dynamics and the kinetics of binding and translation of SMC complexes on the chromatin. This allows for an explicit treatment of motor processivity (Fig. 1*A*). Here, the model relies upon introducing a spin-like indicator $\{s_{ij}\}$, referred to as the *bridging index*, which indicates the crosslinking state between beads i and j. The binding of an SMC motor to the DNA depends on the separation of two beads $r_{ij} = |\mathbf{r}_i - \mathbf{r}_j|$ and is characterized by a grappling probability $\mathcal{C}(r_{ij})$ (23). Once an SMC motor binds to the chromatin fiber, the bridging index s_{ij} switches from 0 (unbound) to 1 (bound) and can bring beads i and j together into closer proximity by a certain distance l along their connecting unit vector $\hat{\mathbf{r}}_{ij}$. The motor remains associated with the fiber for a finite residence time τ, during which it continues to extrude processively without requiring rebinding. After a time τ, the SMC motor dissociates from the fiber, and the bridging index reverts from 1 back to 0. The reaction channels of binding and detachment on the pair (i,j) are denoted as $\mathbf{s}^{ij+}$ and $\mathbf{s}^{ij-}$.

The motors also slide along the chain to extrude loops in a more efficient manner (30–32). After a sliding event, the bridging index of the previously occupied pair switches from 1 to 0, while that of the newly occupied pair switches from 0 to 1 that can proceed either in a one-sided or two-sided manner and may be deterministic or diffusive (19, 33) (Fig. 1*B*). At the 50 kb resolution of the Hi-C map, the symmetric two-sided and ratchet-like (deterministic) model is generally regarded as the one that best describes the mechanism. In this case, a motor-occupied pair (i,j) can take a single outward step, becoming bound on $(i-1, j+1)$ while leaving (i,j) unoccupied. The corresponding hopping reaction channel can be denoted as $\mathbf{s}^{ij\to i-1,j+1}$ (*Materials and Methods*). Without loss of generality, our model can describe other sliding mechanisms by defining corresponding reaction channels. Although the present formalism itself is not tied to a specific coarse-graining level, in the simulations below we use a coarse-grained mapping in which each bead represents a chromatin segment of order $\sim$ 50 kb, consistent with Hi-C resolution and previous chromatin polymer models such as the MiChroM model (26–28). The corresponding simulation time is interpreted as an effective coarse-grained dynamical scale (24, 34). Motor action on shorter sequence scales is not excluded, which might effectively renormalize parameters of this bead-level description.

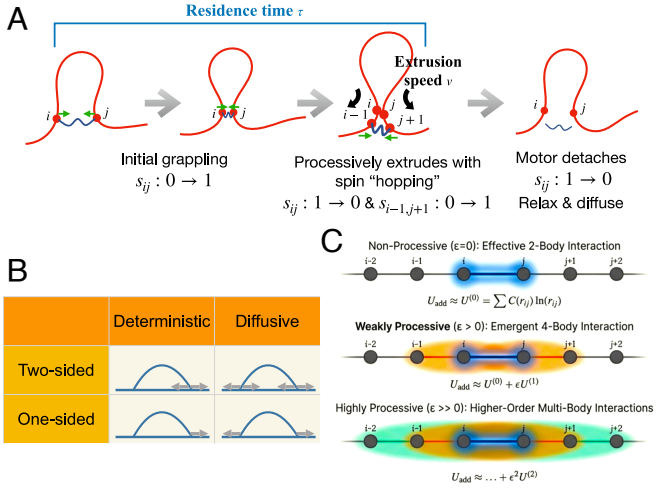

Fig. 1. (*A*) A schematic diagram of the processive grappling motors with deterministic, two-sided extrusion. (*B*) The different mechanisms of the one-sided/two-sided and deterministic/diffusive extrusions in the sequence space. (*C*) Schematic representation for the multibody, cooperative interaction induced by the processive motorization.

Processive grappling events naturally lead to a history dependence of motor activity. We can write down a Master equation for the evolution of the joint distribution of the polymer configuration and the bridging indices

$$\partial_t \Psi_t(\mathbf{r},\mathbf{s}) = [\mathcal{L}_{\rm eq} + \sum_{i<j} \mathcal{L}_{\rm NE}^{(ij)}]\Psi_t(\mathbf{r},\mathbf{s}) \qquad [1]$$

with $\mathcal{L}_{\rm NE} = \mathcal{L}_{\rm NE,r} + \mathcal{L}_{\rm NE,s}$. Here, $\mathcal{L}_{\rm eq} = D\sum_k \nabla_{\mathbf{r}_k}\cdot[\nabla_{\mathbf{r}_k} + \beta\nabla_{\mathbf{r}_k}U(\mathbf{r})]$ represents the ordinary Fokker–Planck operator for the configurational dynamics with D the diffusion constant and $U(\mathbf{r})$ the energy landscape. k indexes the polymer beads, and the sum $\sum_k$ denotes the sum over all bead coordinates. The nonequilibrium operator $\mathcal{L}_{\rm NE}$ consists of two components: the grappling operator $\mathcal{L}_{\rm NE,r}$ and the crosslinking operator $\mathcal{L}_{\rm NE,s}$. $\mathcal{L}_{\rm NE,r}$ acts on the chromatin conformation $\{\mathbf{r}\}$, describing the structural modifications of the chain induced by motor-mediated grappling. In contrast, $\mathcal{L}_{\rm NE,s}$ acts on the bridging index variables $\{\mathbf{s}\}$. It captures the dynamical changes of motor states, including binding, detachment, and hopping events. Both operators $\mathcal{L}_{\rm NE,r}$ and $\mathcal{L}_{\rm NE,s}$ are generally non-Hermitian, since neither the grappling dynamics nor the motor kinetics obey detailed balance. On the one hand, the chromatin conformation dynamics clearly depends on the bridging state of the motors; on the other hand, the initial binding of motors is determined by the distances between bead pairs. This mutual dependence implies that chromatin dynamics and motor kinetics are intrinsically coupled and cannot be completely separate.

We first write down the operator for the grappling events between all the bound crosslinkers,

$$\mathcal{L}_{\rm NE,r}^{(ij)}\Psi(\mathbf{r},\mathbf{s}) = \kappa_p \iint d\mathbf{r}_i' d\mathbf{r}_j' \left\{ G_{+1}^{(ij)}(\mathbf{r},\mathbf{r}',\mathbf{s}) - G_{-1}^{(ij)}(\mathbf{r},\mathbf{r}',\mathbf{s}) \right\}, \qquad [2]$$

where the kernels are

$$G_{\sigma=\pm1}^{(ij)}(\mathbf{r},\mathbf{r}',\mathbf{s}) = \delta_\pm\, e^{-\sigma\vartheta\beta\Delta U} \times \begin{cases} s_{ij}\Psi(\mathbf{r}',\mathbf{s}) & \sigma=+1 \\ s_{ij}\Psi(\mathbf{r},\mathbf{s}) & \sigma=-1 \end{cases}.$$

Here, $\Delta U = U(\mathbf{r}) - U(\mathbf{r}')$ is the free energy difference and $\delta_\pm = \delta(\mathbf{r}_i - \mathbf{r}_i' \mp \mathbf{l}_{ij})\delta(\mathbf{r}_j - \mathbf{r}_j' \pm \mathbf{l}_{ij})\prod_{k\neq i,j}\delta(\mathbf{r}_k - \mathbf{r}_k')$ with $\mathbf{l}_{ij} = l\hat{\mathbf{r}}_{ij}$. The delta functions $\delta_\pm$ enforce the local update of polymer configurations associated with a grappling event, which constrains the posttransition coordinates $\mathbf{r}$ and $\mathbf{r}'$ such that only the positions of the two involved beads i and j are updated by a displacement $\pm\mathbf{l}_{ij}$, while all other bead coordinates remain unchanged. The subtraction of the $\sigma = \pm1$ kernel represents the flux-in term and the flux-out term. The pairwise grappling events occur at a rate κ_p in a processive manner whenever $s_{ij} = 1$, and they proceed until the motor dissociates, without altering the bridging index. The apparent reaction rates depend on the motor susceptibility ϑ, an intrinsic molecular property that characterizes how the motor kinetics respond to applied forces. When $\vartheta = 0$, the motor is completely adamant and insensitive to external loads, as assumed in many models of active matter. However, experiments on cohesin and condensin demonstrate that SMC complexes stall under extremely weak opposing forces, indicating that they are sensitive rather than adamant (3, 13, 14).

Downloaded from https://www.pnas.org by CAS University of Science and Technology of China USTC on May 29, 2026 from IP address 218.22.21.23.

This ΔU-dependence of motors does not merely renormalize effective rates, but can generate qualitatively distinct conformational responses, such as local stretching or compression and the fractal-globule characteristic of interphase chromosomes (23, 25).

Second, we turn to the motor kinetics and write down the crosslinking operator

$$\mathcal{L}^{(ij)}_{\mathrm{NE,s}}\Psi(\mathbf{r},\mathbf{s}) = \underbrace{\kappa_b\left[s_{ij}\mathcal{C}(r_{ij})\Psi(\mathbf{r},\mathbf{s}^{ij-}) - s'_{ij}\mathcal{C}(r_{ij})\Psi(\mathbf{r},\mathbf{s})\right]}_{\text{initial binding } 0\to 1} + \underbrace{\tau^{-1}\left[-s_{ij}\Psi(\mathbf{r},\mathbf{s}) + s'_{ij}\Psi(\mathbf{r},\mathbf{s}^{ij+})\right]}_{\text{detachment } 1\to 0} + \underbrace{v\mathcal{L}^{(ij)}_{\mathrm{slide}}\Psi(\mathbf{r},\mathbf{s})}_{\text{motor sliding}} \quad [3]$$

with $s'_{ij} = 1 - s_{ij}$ the reversed spin. On the right hand side, the first term describes the initial binding event with κ_b the binding rate, and the second term describes the dissociation of bound motors. The third term models the motor sliding as a new "spin-hopping" channel, where v is the extrusion speed (*Materials and Methods*). Multiple factors, including the duty cycle of the power-stroke, chromatin tension, crowding, fatigue, and obstacles, among others, slow down or speed up the sliding process (35, 36). Presently, we will use a constant rate approximation. For isolated motors, the average loop length is $\langle L(t)\rangle = 2\varepsilon$, where $\varepsilon = v\tau$ is the motor processivity. In this coarse-grained description, ε measures the typical extrusion distance relative to the underlying polymer scale. Interphase cohesin typically corresponds to smaller effective ε, whereas mitotic condensins correspond to larger ε, reflecting their larger loop sizes. Boundary sites (i, j) at the chain ends with $i = 1$ or $j = N$ simply have no inflow contribution. In the occupancy-variable-only representation, the hopping term generates ballistic moving waves of occupied bonds, whose mean–field continuum limit reduces to a Burgers-type equation (37). When two motors extrude toward one another, the corresponding hopping currents can mutually block each other if the target state $(i-1, j+1)$ is already occupied. This situation naturally invites analysis using exclusion-process methods, where interesting phenomena such as shock fronts, traffic jams, and pile-ups can emerge (38, 39).

Theoretical Treatment

Experiments currently measure only the statistical configurational properties of the chromatin chain, not the bridging indices. Contact probabilities inferred from Hi-C (1) and distance distributions measured by FISH (40) serve as canonical observables. Because chromatin dynamics and motor kinetics are coupled in a highly nontrivial manner, SMC motors effectively constitute an active bath, motivating a projection–operator approach in which motor occupancies are averaged over to produce memory kernels for the chain motion. Projecting over all bridging indices in Eq. **1** yields the following evolution equation for the marginal configurational density $P(\mathbf{r}, t) = \sum_{\mathbf{s}}\Psi(\mathbf{r},\mathbf{s}, t)$:

$$\partial_t P(\mathbf{r}, t) = \mathcal{L}_{\mathrm{eq}}P(\mathbf{r}, t) + \kappa\sum_{i<j}\iint d\mathbf{r}'_i d\mathbf{r}'_j \times\left[\delta_+ e^{-\vartheta\beta\Delta U}c^{\Theta}_{ij}(\mathbf{r}', t)P(\mathbf{r}', t) - \delta_- e^{\vartheta\beta\Delta U}c^{\Theta}_{ij}(\mathbf{r}, t)P(\mathbf{r}, t)\right], \quad [4]$$

where $\kappa = \kappa_p\kappa_b\tau$ is the composite grappling rate and c^{Θ}_{ij} denotes the (conditional) bridging density field

$$\kappa_b\tau c^{\Theta}_{ij}(\mathbf{r}, t) = \frac{Q_{ij}(\mathbf{r}, t)}{P(\mathbf{r}, t)}, \qquad Q_{ij}(\mathbf{r}, t) = \sum_{\mathbf{s}} s_{ij}\Psi(\mathbf{r},\mathbf{s}, t),$$

where $Q_{ij} = \mathrm{Prob}[\mathbf{r}, t; s_{ij} = 1]$ is the joint density of conformation $\mathbf{r}$ and the occupancy s_{ij}. We see that following the evolution of P requires some type of closure. As written P remains coupled to the auxiliary fields $c^{\Theta}_{ij}(\mathbf{r}, t)$, which depend on the global conformation and are explicitly time-dependent. To obtain a useful moment-based closure, we then multiply Eq. **1** by s_{ij} and sum over all motor occupation states to get the evolution of the joint field Q_{ij} (*Materials and Methods*). Combining the evolution equations for P and Q yields the self-consistent generalized Master equation (GME),

$$\partial_t P(\mathbf{r}, t) = \mathcal{L}_{\mathrm{eq}}P(\mathbf{r}, t) + \left[\mathcal{J}e^{t\mathbf{A}}\mathbf{Q}^0\right](\mathbf{r}) + \kappa\sum_{i<j}\sum_{m=0}\int_0^t dt' \iint d\mathbf{r}'_i d\mathbf{r}'_j\Big[\delta_+ e^{-\vartheta\beta\Delta U}\mathcal{K}_m(t-t')\mathcal{C}(r'_{i+m,j-m})P(\mathbf{r}', t') - \delta_- e^{\vartheta\beta\Delta U}\mathcal{K}_m(t-t')\mathcal{C}(r_{i+m,j-m})P(\mathbf{r}, t')\Big], \quad [5]$$

where m is the number of extrusion steps, and the memory kernel is $\mathcal{K}_m(t) = e^{-\alpha t}(vt)^m/(m!\tau)$ with $\alpha = \tau^{-1} + v$. The second term on the right-hand side of Eq. **5** accounts for contributions from the initial crosslinks $\mathbf{Q}^0$, where the exact expression is presented in *SI Appendix*, section 1. In most applications, we will assume no motors are bound at $t = 0$, so this term vanishes; however, in specific contexts–e.g., exit from mitosis (41–43)–this term can dominate. The third term contains a Gamma-distributed memory kernel that encodes the probability for a grappling event with a complex history to arrive at the current pair by undergoing m steps of extrusion and concomitant polymer relaxation, and to flow into or out of the present location via continued pulling. Summing over all values of m yields the total historical flux weight. The memory kernel $\mathcal{K}_m(t)$ also indicates there is an active, viscoelastic-like response, which can be interpreted as motor-modulated rheology (44, 45). In the Laplace domain, $\tilde{\mathcal{K}}_m(s) = \tau^{-1}v^m(s+\alpha)^{-(m+1)}$ and $\sum_{m\geq 0}\tilde{\mathcal{K}}_m(s) = (\tau s+1)^{-1}$. Two limiting regimes clarify the physics: (i) there is weak processivity when $\varepsilon \ll 1$, in which case the weight is concentrated at $m = 0$ and the kernel is nearly single-exponential (quasi-Markovian); (ii) there is strong processivity when $\varepsilon \gg 1$, in which case higher-m sectors become populated, generating long-range, time-retarded couplings in the configurational dynamics. Eq. **5** furnishes a motor-free simulation framework in which the eliminated motor variables now enter solely through the memory kernel.

Following Wang and Wolynes (46), we expand the probability distribution function in powers of the step size l up to the quadratic order, where the GME (Eq. **5**) will be mapped into a corresponding generalized Fokker–Planck equation (GFPE). From this GFPE, we can identify pairwise spatiotemporal effective diffusion and temperature fields as signatures of the emergent hydrodynamic behavior induced by processive motorization (*Materials and Methods*). More importantly, the processive grappling immediately leads to effective attractive interactions:

$$U_{\mathrm{add}}(\mathbf{r}, t) \simeq \frac{\Delta}{\beta}\sum_{i<j}c^{\Theta}_{ij}(\mathbf{r}, t)\ln r_{ij}, \qquad \Delta = \kappa l^2/D \quad [6]$$

Downloaded from https://www.pnas.org by CAS University of Science and Technology of China USTC on May 29, 2026 from IP address 218.22.21.23.

with Δ the Péclet number. The bridging density field c_{ij}^{Θ} depends both on the *overall* configuration and on time

$$c_{ij}^{\Theta}(\mathbf{r},t)=\frac{1}{\tau}\sum_{m=0}\int_0^t dt'\, e^{-\alpha t'}\frac{(vt')^m}{m!}\mathcal{C}(r_{i+m,j-m}). \qquad [7]$$

Eqs. **6** and **7** show that the effective energy landscape U_{add} is a non-pairwise-additive, many-body potential, because the energy associated with a pair (i,j) depends on the neighboring distances $\{r_{i+m,j-m}\}$. The resulting cooperative attraction arises naturally from processive loop extrusion without requiring any multivalence of the motor-binding: When a neighboring pair is motor-bound, the motor can "tunnel" onto the target pair with a probability set by the processivity ε. This facilitated capture couples adjacent pairs and enhances local binding, analogous to the zippering of DNA helices (47). Such cooperative multibody interactions can reshape the higher-order contact network of chromosomes (48–50). Only in the zero processivity limit $v=0$, does the conditional bridging probability become strictly pairwise while history dependent, arising from a causal convolution $c_{ij}^{\Theta}(r_{ij},t)=\tau^{-1}\int_0^t dt' e^{-t'/\tau}\mathcal{C}(r_{ij})$, which encodes a time-delayed echo of prior grappling events–mathematically akin to diffusion-mediated chemotaxis kernels (51). Such retardation facilitates strong loop formation and even causes coherent motion (52, 53). Further, if we take the limit $\tau\to 0$, then $c_{ij}^{\Theta}(\mathbf{r},t)\to\mathcal{C}(r_{ij}(t))$, we recover the Markovian model from our previous work (23).

To further illustrate the multibody interactions, we can expand Eq. **7** in powers of the processivity ε , and the resulting terms can be systematically decomposed order by order (*Materials and Methods*):

$$U_{\text{add}}=\frac{\Delta}{\beta}\Big[U^{(0)}+\varepsilon U^{(1)}+\varepsilon^2U^{(2)}+O(\varepsilon^3)\Big], \qquad [8]$$

where

$$\begin{aligned}U^{(0)}&=\sum_{i<j}\mathcal{C}(r_{ij})\ln r_{ij}, \quad \text{(2-body)}\\ U^{(1)}&=\sum_{i<j}\mathcal{C}(r_{ij})\ln\frac{r_{i-1,j+1}}{r_{ij}}, \quad \text{(4-body)}\\ U^{(2)}&=\sum_{i<j}\mathcal{C}(r_{ij})\ln\frac{r_{i-2,j+2}\,r_{ij}}{r_{i-1,j+1}^2} \quad \text{(6-body)}.\end{aligned} \qquad [9]$$

The zeroth-order expansion $U^{(0)}$ yields an explicit pairwise attraction that exists whenever the motor residence time τ is finite–even for nonprocessive motors ($\varepsilon=0$), see Fig. 1*C*. Physically, this contribution arises from time-averaged transient bridging events and thus represents an emergent equilibrium-like attraction generated by nonequilibrium motor activity. We see that this contribution provides a bridging-induced attraction (54), which promotes both chromatin compaction and phase separation (55–57). Particularly, it can also capture the role of nonprocessive cohesin during mitosis, which forms links between the distal portions of chromatin loops anchored by axial condensin (18, 58). Previously, we have shown in the nonprocessive case that this term provides a physical mechanistic basis for the so-called ideal chromosome potential (23) inferred from Hi-C data in energy-landscape-based methods, where the effective pair potentials were learned from Hi-C data (26–28).

Expanding further, now, at first order in processivity ε, the effective interaction $U^{(1)}$ involves four monomers and compares the loop size before and after a single extrusion step (Fig. 1*C*). This term therefore encodes correlations between nearby extrusion configurations and constitutes the leading nonequilibrium correction arising from motor memory along the polymer sequence. Its existence relies on directional extrusion; for symmetric stepping kernels, odd-order contributions vanish. At second order, $U^{(2)}$ involves six monomers and depends on a discrete second difference of the logarithmic distance along the extrusion direction (Fig. 1*C*). This structure reflects the motor's sensitivity not only to the local change in loop sizes, but also to its variation across successive steps, effectively probing the curvature of the genomic energy landscape. As the order increases, the many-body terms become increasingly long-ranged and collective, favoring more complex organizational motifs and amplifying correlations over large genomic distances. Processivity turns local motor stepping into a hierarchy of emergent many-body interactions, rather than merely renormalizing pairwise forces.

We estimate the energetic importance of processivity-induced many-body interactions by averaging $U^{(0),(1),(2)}$ over a 3D Gaussian (Rouse) chain ensemble (*SI Appendix*, section 4). For a segment separation s, Gaussian statistics imply that $\langle\ln r(s)\rangle\approx\frac{1}{2}\ln s$, yielding closed-form discrete averages $\langle\ln[r(s+2)/r(s)]\rangle=\frac{1}{2}\ln[(s+2)/s]$ and $\langle\ln[r(s+4)r(s)/r(s+2)^2]\rangle=\frac{1}{2}\ln[s(s+4)/(s+2)^2]$. With $\mathcal{C}(s)\propto s^{-1.1}$ and a physically motivated ultraviolet cutoff $s_{\min}=2$ (one extrusion step), we obtain $|U_{4\text{body}}|/|U_{2\text{body}}|\approx 0.03\varepsilon$ and $|U_{6\text{body}}|/|U_{2\text{body}}|\lesssim 1\%\times\varepsilon^2$ under the reference Gaussian ensemble. For cohesin with low processivity $\varepsilon\sim 1$ to 2, pairwise interactions may be sufficient to describe the system. However, for condensin I with higher processivity $\varepsilon\sim 2$ to 5, motor-induced multibody cooperative interactions must be taken into account. For condensin II with $\varepsilon\sim 10$ to 100, the multibody interactions even dominate the total energy.

The Self-Consistent Equation and Shapes of Contact Probabilities

To theoretically elucidate how the microscopic dynamics of molecular motors (e.g., processivity and directional symmetry) determines the macroscopic 3D topological scaling of chromosomes, we incorporate finite motor processivity ε into our previously established self-consistent equation (23). Following our previous work, we first average the configuration-dependent grappling probability over the polymer conformational ensemble to obtain a purely sequence-dependent grappling probability as $c(i,j)=\langle\mathcal{C}(r_{ij})\rangle$. By assuming a homogeneous polymer chain, this sequence-dependent grappling probability becomes solely a function of the genomic separation $s=|i-j|$, which we denote as $\mathscr{C}(s)=c(i,j)$.

By converting this discrete sequence-dependent probability into a continuum differential-operator representation, we reveal that the macroscopic topological scaling of chromosomes is fundamentally dictated by the microscopic symmetry of the loop-extruding motors. For symmetric, deterministic extrusion (only loop elongation without shrinkage), the motor processivity introduces a first-order gradient correction, yielding the apparent grappling probability $\bar{c}^{\Theta}(s)\approx(1-2a\varepsilon\partial_s)\mathscr{C}(s)$, where a is the lattice spacing. Substituting this into the mean-field closure yields the full self-consistent equation:

$$\frac{\mathscr{C}(s)}{B}=\left[|s|(1-Q\mathcal{C}_T)+Q\int_0^s\big[(1-2a\varepsilon\partial_x)\mathscr{C}(x)\big](s-x)dx\right]^{-\frac{3}{2}}, \qquad [10]$$

Downloaded from https://www.pnas.org by CAS University of Science and Technology of China USTC on May 29, 2026 from IP address 218.22.21.23.

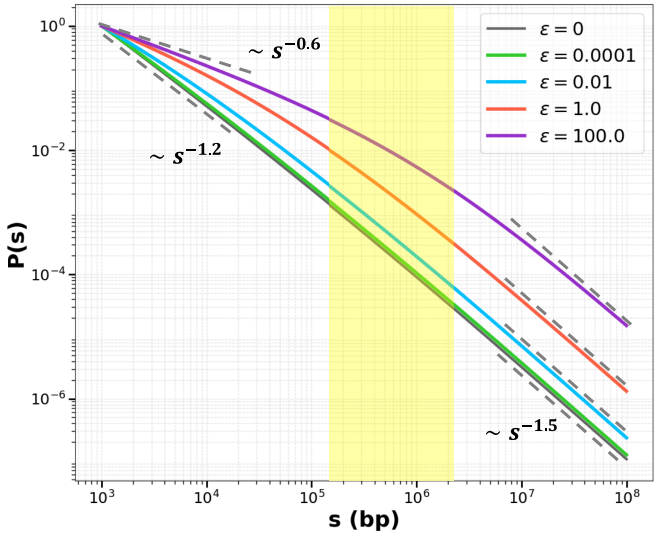

Fig. 2. The chromosomal contact probability $P(s)$ under two-sided, deterministic extrusion (only elongation without shrinkage). We show the numerical solutions of the self-consistent equations when $Q = 0.13$. The introduction of processivity $\epsilon > 0$ induces a first-order gradient correction. As ϵ increases, the characteristic -1.2 power-law decay at short scales is gradually replaced by a much shallower -0.6 scaling regime. The scaling recovers to the Rouse limit $\gamma = 1.5$ at large genomic separations s. The dashed lines indicate the characteristic power-law slopes, and the yellow rectangle indicates the region where the crossover of power-law decay occurs.

where $B = 2\sqrt{6/\pi}(2l/b_G)^3$ is a dimensionless parameter that depends on the ratio of grappling distance l to the effective Kuhn length b_G. $Q = (\vartheta - \frac{1}{2})\Delta$ is the nonequilibrium factor that quantifies the net bias induced by active motor-driven grapplings. It vanishes either in the weak-activity limit $\Delta \to 0$ or when grapplings obey detailed balance $\vartheta = 1/2$. $\mathcal{C}_T = \int d\mathscr{C}(s)$ is the (local) total grappling probability.

Analytically, the self-consistent equation predicts a multi-regime power-law decay for the contact probability $P_c(s) \propto |s|^{-\gamma}$. With the introduction of processivity, the characteristic -1.2 power-law decay at short scales [for $\varepsilon = 0$ (23)] is gradually replaced by a shallower -0.6 scaling regime (*SI Appendix*, section 3). As verified by our numerical integrations (Fig. 2), increasing motor activity ε systematically expands this shallow -0.6 regime. For cohesin during interphase chromosomes ($\varepsilon \sim 1$ to 2), our theory yields an effective power-law exponent of ~ -0.8 to 1.0, i.e., slightly flatter than the experimentally observed scaling -1.1. A likely reason is that we have not included one-sided extrusion or motor slip; both effects would effectively reduce the net processivity (and thus weaken the renormalization of the contact kernel), bringing the predicted decay closer to experiment. This transition predicted by our theory also captures the fundamental shift from interphase chromosomes–where low-processivity cohesins, frequently impeded by CTCF, yield a scaling of -1.1–to mitotic chromosomes, where high-processivity condensin motors operate largely unfettered by CTCF to drive a dominant -0.5 scaling (2, 18, 59).

So far, we have only considered the first-order correction to the renormalization of the contact probability. At high processivity, however, the second-order term becomes relevant and induces an additional flattening of the decay, leading to a plateau behavior (*SI Appendix*, section 3). This effect is confined to very short sequence separations and does not modify the large-scale asymptotic scaling, consistent with what is observed in our simulations (31).

Chromatin Jets

Beyond renormalizing the shapes of contact probabilities, processivity leads to several novel features of chromosomal organization. One such feature is the chromatin jet, a diffuse off-diagonal ridge in Hi-C maps that marks directed loop extrusion from a cohesin loading site (29). These jets suggest the existence of active extrusion anchors and asymmetric propagation of chromatin structures because they are near CTCF sites, which act as barriers that can suppress or deflect jet extension.

In addition to the analytical arguments, we have performed hybrid simulations of chromatin dynamics under processive loop extrusion, explicitly accounting for motor kinetics. To see jets, the motors were allowed to bind only within a focal region (binding probability set to zero elsewhere) located near the chain midpoint (Fig. 3*A*) as suggested by the experiments (29). Once bound, a motor could slide along the chromatin until encountering a CTCF barrier. When motors are sufficiently processive, the simulations lead to antiparallel loop structures (Fig. 3*A*) yielding clear chromatin jet signatures (Fig. 3*B*).

We next simulated systems retaining the interaction (Eq. **9**) terms of increasing order: 2th, 4th, 6th (Fig. 3*C*), so that the polymer evolves under the effective Hamiltonian $U_{\text{eff}} = U + U_{\text{add}}$ with U the original polymer free-energy functional and U_{add} the motor-induced effective interaction derived from Eq. **9**, designed to isolate the structural consequences of the motor-induced interaction. In these simulations, we retain the effective interaction but do not include the state-dependent effective temperature or modified diffusion. These results show that the pairwise interactions alone are insufficient to generate chromatin jets of realistic strength and spatial extent–reminiscent of the way, in active matter, phase separation occurs only when multibody cage effects are included (60, 61). As evident from Eq. **9**, the zeroth-order expansion produces effective attractions confined to the focal region, while the higher-order multibody terms induce cooperative attractions that extend beyond it. Increasing the expansion order systematically broadens the effective interaction range, propagating outward until it reaches the CTCF boundary. The inclusion of many-body interactions

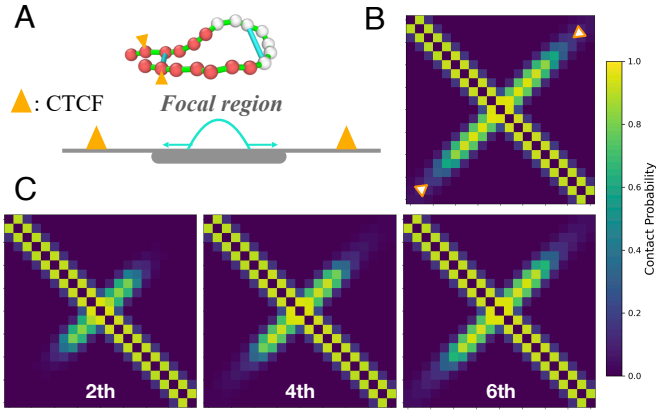

Fig. 3. Simulation of chromatin jets. (*A*) Schematics of the model. Motors can only bind to the focal region and extrude until the CTCF (*Bottom*). The representative antiparallel loop structure of the active simulation based on Eq. **1** (up). Blue: the bound motors. White: the focal region. (*B*) The Hi-C map of the active simulation based on Eq. **1** shows a clear jet effect. Orange triangle: CTCFs. (*C*) The Hi-C maps for simulating the effective system with multibody interactions (Eq. **9**), truncated at different orders: 2th (*Left*), 4th (*Middle*), and 6th (*Right*). Parameters are $\varepsilon = 1$ and $\kappa = 20$ ($\kappa_b = 20$, $\kappa_g = 1$, $\tau = 1$, and $v = 1$).

Downloaded from https://www.pnas.org by CAS University of Science and Technology of China USTC on May 29, 2026 from IP address 218.22.21.23.

suppresses fluctuations and stabilizes loop structures, much as the nonadditive multibody hydrophobic effects provide larger barriers in protein folding (62–64). The effective interactions provide an alternative framework for describing systems with finite processivity without explicitly simulating motors. The hierarchy of multibody terms can be truncated at a finite order (e.g., at the $2m$-body level). Interestingly, such a truncated system can be mapped onto a lower-order $2(m-j)$-body truncation description after expanding the focal region by $2j$ sites.

Mitotic Chromosome

We follow our recent work (24) to explore how processive grappling motors shape mitotic chromosomes. The simulated steady-state configurations exhibit rod-like morphology with global helical ordering and symmetry breaking under the action of condensin I and II, consistent with experimental observations and in agreement with predictions from the information-theoretic energy landscape model inferred from Hi-C data (28, 65). Since the processivity of condensins during mitosis extends beyond the range of the leading-order expansion, the residence time and extrusion speed no longer act in a simple composite manner. To capture these nonlinear effects explicitly, we therefore directly simulate Eq. **1**, in which motor processivity is incorporated as an explicit dynamical variable. Through these simulations, we find that the processivity of condensin II strongly shapes the global architecture of mitotic chromosomes by driving global compaction (66, 67) (*Materials and Methods*). First, to quantify the mechanical consequences of this compaction, we computed the mean-squared displacement (MSD) averaged over all beads. The long-time plateau of the MSD provides a measure of the characteristic vibrational amplitude of each bead around its reference position–that is, the effective cage size*–which reflects the rigidity of the chromosomal scaffold against thermal and mechanical perturbations (68). We plotted the phase diagram of the plateau value $\mathcal{A}$ as a function of the condensin II grappling rate κ_p^{II} and residence time τ (Fig. 4*A*). When τ approaches the maximal value observed in experiments for condensins, the corresponding characteristic cage size computed by the plateau value is smaller than the typical Lindemann length ($\sim 0.1\sigma$ with σ the average bead spacing) found in melting, indicating a crystal-like organization. As τ decreases, this length will exceed the Lindemann threshold. Introducing motor processivity also causes this characteristic length to increase progressively with extrusion speed v (*SI Appendix*, Figs. S3 and S4). This trend signifies a structural transition from a crystalline to a soft-crystalline, and ultimately to a liquid-crystalline state, reflecting the competition between bridging-induced vulcanization (57) and extrusion-driven fluidization (69). We next examined how motor processivity affects the global helical order, i.e., the large-scale cholesteric-like organization, quantified by the intensity I_g of the low-frequency peak in the Fourier spectrum of the orientational order parameter O_{OP} (*Materials and Methods*). The phase diagram of I_g shows that global helical order decreases with increasing the residence time τ, but increases with increasing the extrusion speed v (Fig. 4*B*). This behavior reflects two competing effects: Long-lived motors act as transient quenched disorder, creating crosslinks that disrupt global helical order, whereas motor-driven extrusion accelerates local stress relaxation and redistributes loop sizes, thereby removing these long-lived defects. We believe that the experimental measurement of these order parameters will provide valuable insight into chromosome symmetry breaking.

*When the MSD shows a long-time plateau, the beads are confined to small vibrations around fixed reference positions, akin to oscillations in a crystalline lattice rather than free diffusion, and the plateau height reflects the amplitude of these vibrations.

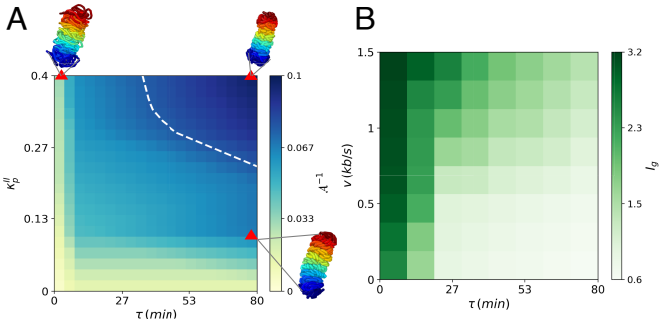

Fig. 4. Phase diagrams for the order parameters during mitosis. (*A*) The inverse of the plateau of bead-averaged MSDs $\mathcal{A}^{-1}$ as a function of the condensin II grappling rate κ_p^{II} and residence time τ with the condensin I grappling rate $\kappa_p^{I} = 0.4$ and $v = 0$. The white dashed line represents the phase boundary when the plateau value approaches the Lindemann length. The representative configuration corresponding to the red triangle in the phase diagram is shown alongside the diagram. (*B*) The global helical order, quantified by the intensity (I_g) of the low-frequency peak in the Fourier spectrum of the orientational order parameter O_{OP} as a function of the residence time τ and the extrusion speed v with $\kappa_p^{I} = \kappa_p^{II} = 0.4$.

Discussion

We have presented a mechanistic model for studying how SMC motor processivity influences macroscopic chromatin organization. Our analysis demonstrates how processive loop extrusion gives rise to effective, cooperative many-body interactions, and offers a controlled coarse-graining strategy linking explicit motor-driven dynamics to reduced effective energy landscape models. In particular, we show how motor processivity regulates the shapes of contact probabilities, the emergence of chromatin jets, and the structural transitions of mitotic chromosomes. Our framework can be extended to other persistent active biological systems, such as the cytoskeleton, where processivity may regulate the onset of spontaneous flows (70, 71), oscillations (72), or contractility (73, 74).

Materials and Methods

The Reaction Channel and Operator for Sliding. The reaction channels of binding and detachment can be defined as (Fig. 1*A*)

$$\mathbf{s}^{ij+} := \begin{cases} s_{ij} = 1 \\ s_{kl} = s_{kl} \end{cases}, \quad \mathbf{s}^{ij-} := \begin{cases} s_{ij} = 0 \\ s_{kl} = s_{kl} \end{cases}$$

with $(k, l) \neq (i, j)$. For the two-sided, deterministic sliding, the reaction channel is (Fig. 1*A*)

$$\mathbf{s}^{i+1,j-1\to ij} := \begin{cases} s_{ij} = 0, \\ s_{i+1,j-1} = 1, \\ s_{kl} = s_{kl} \quad \text{otherwise} \end{cases}$$

We can then write down the sliding operator $\mathcal{L}_{\text{slide}}^{(ij)}$ acting on a given pair (i, j), describing the one-way outward sliding process $(i{+}1, j{-}1) \to (i, j) \to (i{-}1, j{+}1)$

$$\begin{aligned} \mathcal{L}_{\text{slide}}^{(ij)}\Psi(\mathbf{r}, \mathbf{s}) = {} & s_{ij}s'_{i+1,j-1}\Psi(\mathbf{r}, \mathbf{s}^{i+1,j-1\to ij}) \\ & + s'_{ij}s_{i-1,j+1}\Psi(\mathbf{r}, \mathbf{s}^{ij\to i-1,j+1}) \\ & - s'_{ij}s_{i+1,j-1}\Psi(\mathbf{r}, \mathbf{s}) - s_{ij}s'_{i-1,j+1}\Psi(\mathbf{r}, \mathbf{s}), \end{aligned} \quad [11]$$

Downloaded from https://www.pnas.org by CAS University of Science and Technology of China USTC on May 29, 2026 from IP address 218.22.21.23.

where $s'_{ij} = 1 - s_{ij}$. The factors in the form of $(1-s)$ will enforce exclusion constraints (preventing hops into already-occupied targets). In the dilute limit, these projection factors can be approximated as unity. At $i = 1$ or $j = N$, one sets $s_{i+1,j-1} \equiv 0$ or $(1 - s_{i-1,j+1}) \equiv 0$, automatically removing out-of-bounds transitions. If we consider the bidirectional extrusion, the above expression should be symmetrized by adding the terms for the inward channel $(i-1, j+1) \to (i, j)$ and $(i, j) \to (i+1, j-1)$.

Experiments and theoretical analyses have revealed a diversity of mechanistic behaviors underpinning loop extrusion. The detailed mechanisms of SMC motors allow them to act either in a one-sided or two-sided manner and may be deterministic or diffusive (Fig. 1*B*). Classical polymer models often treat loop extruders as two-sided motors that reel in DNA symmetrically from both legs to enlarge loops, consistent with early Hi-C based simulations of chromosome organization (19). Recently, direct visualization of individual complexes has shown that many eukaryotic SMC motors extrude DNA asymmetrically in a one-sided fashion on experimental timescales, with the opposite leg remaining anchored (33). Frequent direction switches during asymmetric extrusion can produce an apparent symmetric behavior over longer intervals, suggesting that symmetric loop growth may emerge from temporally alternating one-sided activity rather than simultaneous bidirectional translocation (33). In addition, at a mechanistic level, several conceptual models have been proposed to explain how ATP hydrolysis drives translocation and loop enlargement. In Brownian ratchet models, conformational changes of the SMC ring bias thermal motions to preferentially enlarge loops in discrete steps, providing an ATP-dependent ratcheting mechanism for directed extrusion (75). Alternative frameworks emphasize diffusive components, where DNA segments within or adjacent to SMC rings can transiently slide and be rectified into loop growth either through binding kinetics or collective osmotic effects in ensembles of slip-link-like proteins (37, 76). These ratchet-like versus diffusive mechanisms reflect active versus quasi-passive interpretations of loop enlargement, highlighting that loop extrusion may combine both motor-driven translocation and stochastic strand dynamics depending on the specific SMC complex and loading context. Overall, while the basic phenomenon of processive loop expansion is widely accepted, our understanding of the precise symmetry and physical mechanism of SMC motors continues to be refined with ongoing structural and single-molecule studies. Our main results can be extended to other extrusion mechanism cases, such as one-sided extrusion (*SI Appendix*, section 3).

The Evolution of the Joint Field. The dynamical evolution of Q_{ij} can be obtained by multiplying Eq. **1** by s_{ij} and then summing over all motor occupation states. To obtain the final closure, we can neglect higher-order moments, analogous to what is done when truncating the BBGKY hierarchy (77–80). We also neglect the contribution from equilibrium relaxation and processive grappling, which primarily reshapes the P rather than the occupancies; hence, it may be neglected at leading order. The detailed derivations and analysis are included in *SI Appendix*, section 1. In conclusion, the Q_{ij} dynamics read:

$$\partial_t Q_{ij}(\mathbf{r}, t) \simeq \underbrace{-\tau^{-1} Q_{ij}(\mathbf{r}, t)}_{\text{detachment}} + \underbrace{\kappa_b \mathcal{C}(r_{ij})[P - Q_{ij}](\mathbf{r}, t)}_{\text{binding}} + \underbrace{v[Q_{i+1,j-1}(\mathbf{r}, t) - Q_{ij}(\mathbf{r}, t)]}_{\text{motor sliding}}. \quad [12]$$

The first term represents the loss due to motor detachment, while the second term accounts for the gain of bridging occupancy from binding events governed by $\mathcal{C}(r_{ij})$. The third term captures the sliding process, which generates an outward advection of bridging probability along the pair–index lattice. Owing to sliding, Q_{ij} couples to its "upstream" neighbor $Q_{i+1,j-1}$ and in turn feeds its "downstream" neighbor $Q_{i-1,j+1}$. We can use a concise formulation by defining the shift operator H by $(HQ)_{ij} = Q_{i+1,j-1} - Q_{ij}$, stacking pair fields into $\mathbf{Q} = (\cdots, Q_{ij}, \cdots)^\top$, and letting $\mathbf{C} = \mathrm{diag}[\mathcal{C}(r_{ij})]$. The evolution equation for the joint field $Q_{ij}(\mathbf{r}, t)$ yields

$$\partial_t \mathbf{Q} = -\tau^{-1}\mathbf{Q} + \kappa_g \mathbf{C}(P\mathbf{I} - \mathbf{Q}) + vH\mathbf{Q} = \mathbf{A}\mathbf{Q} + \kappa_g \mathbf{C}P, \quad [13]$$

where $\mathbf{A} = -\tau^{-1}\mathbf{I} - \kappa_g \mathbf{C} + vH$ with $\boldsymbol{I}$ the identity matrix. Under the "weak-site-dependence" approximation that the grappling probability varies only weakly between neighboring anchor sites $\mathcal{C}(r_{i\pm1,j\mp1}) \simeq \mathcal{C}(r_{ij})$, $\mathbf{C}$ approximately commutes with the shift H (*SI Appendix*, section 1). By using the formal solution of Eq. **13** and the expansion of the Poisson shifter $[e^{uvH}]_{ij,kl} = e^{-vu}\sum_{m=0} \frac{(vu)^m}{m!}\delta_{k,i+m}\delta_{l,j-m}$, we can obtain the GME (Eq. **5**) in the main text.

The Effective Diffusion, Temperature, and Interaction. When we expand the GME (Eq. **5**) to identify the effective attractive interactions (Eq. **6**), we can also identify the effective diffusion tensor and the effective temperature tensor at the same time

$$\mathbf{D}_{\mathrm{eff},ii} = D\mathbf{I} + \frac{1}{2}\kappa_p l^2 \sum_{j\neq i} c_{ij}^{\Theta} \hat{\mathbf{r}}_{ij}\hat{\mathbf{r}}_{ij}, \quad \mathbf{D}_{\mathrm{eff},ij} = -\frac{1}{2}\kappa_p l^2 c_{ij}^{\Theta} \hat{\mathbf{r}}_{ij}\hat{\mathbf{r}}_{ij}, \quad [14]$$

$$\boldsymbol{\beta}_{\mathrm{eff},ii} = \beta\Big[\mathbf{I} + (\vartheta - \frac{1}{2})\frac{\kappa_p l^2}{D}\sum_{j\neq i} c_{ij}^{\Theta} \hat{\mathbf{r}}_{ij}\hat{\mathbf{r}}_{ij}\Big], \quad \boldsymbol{\beta}_{\mathrm{eff},ij} = 2\vartheta\beta \hat{\mathbf{r}}_{ij}\hat{\mathbf{r}}_{ij}, \quad [15]$$

Both the effective temperature and the effective diffusion coefficients of the chromatin degrees of freedom become state- and time-dependent, being modulated by the globally evolving bridging-density field. This spatiotemporal heterogeneity resembles an unusual hydrodynamic interaction: Fluctuations at one locus feed back nonlocally through motor-mediated occupancy and its memory kernel, thereby violating the equilibrium fluctuation–dissipation theorem in a controlled manner. The magnitude and structure of these effects depend sensitively on motor mechanics, e.g., the susceptibility ϑ and the processivity ε.

To obtain the order-by-order effective multibody interaction (Eq. **9**) from Eq. **6**, we first expand Eq. **7** over the motor processivity ε, yielding (*SI Appendix*, section 2)

$$c_{ij}^{\Theta}(\mathbf{r}) = \sum_{m=0}^{\infty} \underbrace{\frac{\varepsilon^m}{(1+\varepsilon)^{m+1}}}_{w_m(\varepsilon)} \mathcal{C}(r_{i+m,j-m}), \quad \sum_{m\geq 0} w_m = 1. \quad [16]$$

Here, $w_m(\varepsilon)$ is a geometric weight over m. For the interphase phase, one can assume a timescale separation in which the motor kinetics are faster than the polymer dynamics, allowing for quasi-equilibrium. For such a short term memory, we truncate Eq. **16** up to the second order that $c^{\Theta} \simeq \big[I + \varepsilon H + \varepsilon^2 H^2 + O(\varepsilon^3)\big]\mathcal{C}$. Inserting in $U_{\mathrm{add}} \propto \sum_{i<j} c_{ij}^{\Theta} \ln r_{ij}$ and using discrete Abel summation-by-parts (neglecting the boundaries for long chains) yields Eq. **9** in the main text. The ε-expansion is best controlled when the processivity is small compared with the characteristic polymer scale. Larger values of ε correspond to a more strongly nonequilibrium regime where higher-order contributions become important. The magnitudes of the terms depend on the specific extrusion mechanisms through distinct combinatorial pathways. In the two-sided extrusion scenario, nearby crosslinked pairs on both sides can facilitate the capture of a target pair–thus, high-order couplings arise in 4th, 6th, ... orders. By contrast, in a strictly one-sided scheme, the cooperative paths extend in only one direction, and thus nontrivial coupling orders emerge in 3rd, 4th, ... orders. In other words, bidirectional extrusion admits two symmetric propagation channels, enabling even-order cooperative enhancements; one-sided extrusion only admits unidirectional propagation, leading to odd-order dominance in the coupling expansion. The simulation results for the one-sided extrusion mechanism are available in *SI Appendix*.

The Simulation Details of Mitotic Chromosomes. In our mitotic chromosome simulations, the chromatin fiber is modeled as a homopolymer of 1500 beads, with each bead corresponding to the resolution of the Hi-C map (~50 kb). We then present a detailed analysis of how condensin II processivity controls the global structural organization of the mitotic chromosome. The free energy difference ΔU evaluated in the simulations is computed solely

Downloaded from https://www.pnas.org by CAS University of Science and Technology of China USTC on May 29, 2026 from IP address 218.22.21.23.

from the baseline polymer potential and no additional entropic contributions are included. Condensin II processivity is found to be the dominant factor determining the overall architectural features of mitotic chromosomes. Other details of the simulations are provided in *SI Appendix*, section 5. Increasing the residence time of condensin II enhances structural compaction, reducing both the long and short axes of the chromosome, with the most pronounced effect along the longitudinal axis (*SI Appendix*, Fig. S3). In contrast, increasing the extrusion speed v of condensin II leads to a slight expansion of the structure, as faster extrusion accelerates local stress relaxation (*SI Appendix*, Fig. S3). The change in the activity of condensin I (κ_p^I) does not affect our main conclusion (*SI Appendix*, Fig. S4).

In the main text, we quantify the helical ordering of the mitotic chromosome using the orientational order parameter $O_{OP}(i-j)$ (24, 28, 65), which measures the correlation between two unit bond vectors connecting beads $[i, i+4]$ and $[j, j+4]$ (*SI Appendix*, Fig. S1):

$$O_{OP}(i-j) = \langle \mathbf{r}_{i,i+4} \cdot \mathbf{r}_{j,j+4} \rangle. \quad [17]$$

Here, $\mathbf{r}_{i,i+4}$ and $\mathbf{r}_{j,j+4}$ are the unit vectors that point from the i-th to the $i+4$-th locus and from the j-th to the $j+4$-th locus. The bracket $\langle \cdot \rangle$ represents the average over the ensemble of structures. $O_{OP}(i-j)$ exhibits oscillations as a function of genomic distance, reflecting the presence of fiber structures associated with a helical motif in chromosomes. The characteristic frequency and amplitude of these helices can be identified from the Fourier spectrum of $O_{OP}(i-j)$. The spectrum of mitotic chromosome structures displays two distinct peaks, indicating a hierarchical helical organization. The stronger, higher-frequency component corresponds to local helical ordering at shorter genomic distances (80 to 400 kb), arising from condensin I-mediated formation of local loop arrays (2, 24). In contrast, the lower-frequency component reflects a global helical order associated with larger loop sizes (3 Mb) and longer spatial periods, which requires the action of condensin II (2, 24). The intensities of the low-frequency component (global helical order) and high-frequency component (local helical order) are denoted by I_g and I_l, respectively.

Data, Materials, and Software Availability. Codes and example output files are available in https://github.com/CaOaC/Processivity (81) and have been archived in Zenodo at https://doi.org/10.5281/zenodo.20091942 (82). All other data are included in the manuscript and/or *SI Appendix*.

ACKNOWLEDGMENTS. Z.C. and P.G.W. were supported both by the Bullard-Welch Chair at Rice University, grant C-0016, and by the Center for Theoretical Biological Physics sponsored by NSF grant PHY- 2019745.

Author affiliations: [a]Center for Theoretical Biological Physics, Rice University, Houston, TX 77005; [b]Department of Chemical Physics, University of Science and Technology of China, Hefei, Anhui 230026, China; [c]Department of Chemistry, Rice University, Houston, TX 77005; and [d]Department of Physics, Rice University, Houston, TX 77005

1. E. Lieberman-Aiden *et al.*, Comprehensive mapping of long-range interactions reveals folding principles of the human genome. *Science* **326**, 289–293 (2009).
2. J. H. Gibcus *et al.*, A pathway for mitotic chromosome formation. *Science* **359**, eaao6135 (2018).
3. M. Ganji *et al.*, Real-time imaging of DNA loop extrusion by condensin. *Science* **360**, 102–105 (2018).
4. I. F. Davidson *et al.*, DNA loop extrusion by human cohesin. *Science* **366**, 1338–1345 (2019).
5. G. Fudenberg, N. Abdennur, M. Imakaev, A. Goloborodko, L. A. Mirny, "Emerging evidence of chromosome folding by loop extrusion" in *Chromosome Segregation and Structure*, D. Stewart, B. Stillman, Eds. (Cold Spring Harbor Laboratory Press, 2017), vol. 82, pp. 45–55.
6. L. Vian *et al.*, The energetics and physiological impact of cohesin extrusion. *Cell* **173**, 1165–1178 (2018).
7. F. Uhlmann, SMC complexes: From DNA to chromosomes. *Nat. Rev. Mol. Cell Biol.* **17**, 399–412 (2016).
8. B. W. Bauer *et al.*, Cohesin mediates DNA loop extrusion by a "swing and clamp" mechanism. *Cell* **184**, 5448–5464 (2021).
9. C. Dekker, C. H. Haering, J. M. Peters, B. D. Rowland, How do molecular motors fold the genome? *Science* **382**, 646–648 (2023).
10. E. Alipour, J. F. Marko, Self-organization of domain structures by DNA-loop-extruding enzymes. *Nucleic Acids Res.* **40**, 11202–11212 (2012).
11. R. Takaki, A. Dey, G. Shi, D. Thirumalai, Theory and simulations of condensin mediated loop extrusion in DNA. *Nat. Commun.* **12**, 5865 (2021).
12. J. F. Marko, P. De Los Rios, A. Barducci, S. Gruber, DNA-segment-capture model for loop extrusion by structural maintenance of chromosome (SMC) protein complexes. *Nucleic Acids Res.* **47**, 6956–6972 (2019).
13. J. K. Ryu *et al.*, Condensin extrudes DNA loops in steps up to hundreds of base pairs that are generated by ATP binding events. *Nucleic Acids Res.* **50**, 820–832 (2022).
14. Y. Kim, Z. Shi, H. Zhang, I. J. Finkelstein, H. Yu, Human cohesin compacts DNA by loop extrusion. *Science* **366**, 1345–1349 (2019).
15. C. Hoencamp, B. D. Rowland, Genome control by SMC complexes. *Nat. Rev. Mol. Cell Biol.* **24**, 633–650 (2023).
16. P. Mach *et al.*, Cohesin and CTCF control the dynamics of chromosome folding. *Nat. Genet.* **54**, 1907–1918 (2022).
17. J. Lee *et al.*, Kinetic organization of the genome revealed by ultraresolution multiscale live imaging. *Science* **389**, eadx2202 (2025).
18. K. Samejima *et al.*, Rules of engagement for condensins and cohesins guide mitotic chromosome formation. *Science* **388**, eadq1709 (2025).
19. E. J. Banigan, A. A. van den Berg, H. B. Brandão, J. F. Marko, L. A. Mirny, Chromosome organization by one-sided and two-sided loop extrusion. *eLife* **9**, e53558 (2020).
20. B. Chan, M. Rubinstein, Theory of chromatin organization maintained by active loop extrusion. *Proc. Natl. Acad. Sci. U.S.A.* **120**, e2222078120 (2023).
21. A. Goychuk, D. Kannan, A. K. Chakraborty, M. Kardar, Polymer folding through active processes recreates features of genome organization. *Proc. Natl. Acad. Sci. U.S.A.* **120**, e2221726120 (2023).
22. K. E. Polovnikov *et al.*, Crumpled polymer with loops recapitulates key features of chromosome organization. *Phys. Rev. X* **13**, 041029 (2023).
23. Z. Cao, P. G. Wolynes, Motorized chain models of the ideal chromosome. *Proc. Natl. Acad. Sci. U.S.A.* **121**, e2407077121 (2024).
24. Z. Cao, C. Du, Z. Hou, P. G. Wolynes, Motorized chromosome models of mitotic chromosome folding. *Nat. Commun.* **16**, 11085 (2025).
25. Z. Cao, P. G. Wolynes, Chromatin folding through nonuniform motorization by responsive motor proteins. *J. Chem. Phys.* **161**, 224903 (2024).
26. B. Zhang, P. G. Wolynes, Topology, structures, and energy landscapes of human chromosomes. *Proc. Natl. Acad. Sci. U.S.A.* **112**, 6062–6067 (2015).
27. M. Di Pierro, B. Zhang, E. L. Aiden, P. G. Wolynes, J. N. Onuchic, Transferable model for chromosome architecture. *Proc. Natl. Acad. Sci. U.S.A.* **113**, 12168–12173 (2016).
28. B. Zhang, P. G. Wolynes, Shape transitions and chiral symmetry breaking in the energy landscape of the mitotic chromosome. *Phys. Rev. Lett.* **116**, 248101 (2016).
29. Y. Guo *et al.*, Chromatin jets define the properties of cohesin-driven in vivo loop extrusion. *Mol. Cell* **82**, 3769–3780 (2022).
30. A. L. Sanborn *et al.*, Chromatin extrusion explains key features of loop and domain formation in wild-type and engineered genomes. *Proc. Natl. Acad. Sci. U.S.A.* **112**, E6456–E6465 (2015).
31. G. Fudenberg *et al.*, Formation of chromosomal domains by loop extrusion. *Cell Rep.* **15**, 2038–2049 (2016).
32. A. Goloborodko, J. F. Marko, L. A. Mirny, Chromosome compaction by active loop extrusion. *Biophys. J.* **110**, 2162–2168 (2016).
33. R. Barth *et al.*, SMC motor proteins extrude DNA asymmetrically and can switch directions. *Cell* **188**, 749–763 (2025).
34. M. Di Pierro, D. A. Potoyan, P. G. Wolynes, J. N. Onuchic, Anomalous diffusion, spatial coherence, and viscoelasticity from the energy landscape of human chromosomes. *Proc. Natl. Acad. Sci. U.S.A.* **115**, 7753–7758 (2018).
35. I. F. Davidson *et al.*, CTCF is a DNA-tension-dependent barrier to cohesin-mediated loop extrusion. *Nature* **616**, 822–827 (2023).
36. S. K. Nomidis, E. Carlon, S. Gruber, J. F. Marko, DNA tension-modulated translocation and loop extrusion by SMC complexes revealed by molecular dynamics simulations. *Nucleic Acids Res.* **50**, 4974–4987 (2022).
37. C. A. Brackley *et al.*, Nonequilibrium chromosome looping via molecular slip links. *Phys. Rev. Lett.* **119**, 138101 (2017).
38. B. Derrida, An exactly soluble non-equilibrium system: The asymmetric simple exclusion process. *Phys. Rep.* **301**, 65–83 (1998).
39. R. A. Blythe, M. R. Evans, Nonequilibrium steady states of matrix-product form: A solver's guide. *J. Phys. A Math. Theor.* **40**, R333 (2007).
40. D. Huber, L. V. Von Voithenberg, G. V. Kaigala, Fluorescence in situ hybridization (fish): History, limitations and what to expect from micro-scale fish? *Micro Nano Eng.* **1**, 15–24 (2018).
41. K. Abramo *et al.*, A chromosome folding intermediate at the condensin-to-cohesin transition during telophase. *Nat. Cell Biol.* **21**, 1393–1402 (2019).
42. E. M. Hildebrand *et al.*, Mitotic chromosomes are self-entangled and disentangle through a topoisomerase-II-dependent two-stage exit from mitosis. *Mol. Cell* **84**, 1422–1441 (2024).
43. A. Brunner *et al.*, Quantitative imaging of loop extruders rebuilding interphase genome architecture after mitosis. *J. Cell Biol.* **224**, e202405169 (2025).
44. R. Bruinsma, A. Y. Grosberg, Y. Rabin, A. Zidovska, Chromatin hydrodynamics. *Biophys. J.* **106**, 1871–1881 (2014).
45. F. Conforto, A. Valdes, W. Vanderlinden, D. Michieletto, Complex rheology of condensin in entangled DNA. bioRxiv [Preprint] (2025). https://doi.org/10.1101/2025.06.04.657969 (Accessed 15 June 2025).
46. S. Wang, P. G. Wolynes, Communication: Effective temperature and glassy dynamics of active matter. *J. Chem. Phys.* **135**, 051101 (2011).
47. B. H. Zimm, J. Bragg, Theory of the phase transition between helix and random coil in polypeptide chains. *J. Chem. Phys.* **31**, 526–535 (1959).
48. B. Bintu *et al.*, Super-resolution chromatin tracing reveals domains and cooperative interactions in single cells. *Science* **362**, eaau1783 (2018).
49. E. M. Darrow *et al.*, Deletion of dxz4 on the human inactive x chromosome alters higher-order genome architecture. *Proc. Natl. Acad. Sci. U.S.A.* **113**, E4504–E4512 (2016).
50. J. Harju, J. J. Messelink, C. P. Broedersz, Multicontact statistics distinguish models of chromosome organization. *Phys. Rev. E* **111**, 014403 (2025).

Downloaded from https://www.pnas.org by CAS University of Science and Technology of China USTC on May 29, 2026 from IP address 218.22.21.23.

51. C. Xue, H. G. Othmer, Multiscale models of taxis-driven patterning in bacterial populations. *SIAM J. Appl. Math.* **70**, 133–167 (2009).
52. A. Zidovska, D. A. Weitz, T. J. Mitchison, Micron-scale coherence in interphase chromatin dynamics. *Proc. Natl. Acad. Sci. U.S.A.* **110**, 15555–15560 (2013).
53. A. Goychuk, D. Kannan, M. Kardar, Delayed excitations induce polymer looping and coherent motion. *Phys. Rev. Lett.* **133**, 078101 (2024).
54. C. A. Brackley, S. Taylor, A. Papantonis, P. R. Cook, D. Marenduzzo, Nonspecific bridging-induced attraction drives clustering of DNA-binding proteins and genome organization. *Proc. Natl. Acad. Sci. U.S.A.* **110**, E3605–E3611 (2013).
55. J. K. Ryu *et al*., Bridging-induced phase separation induced by cohesin SMC protein complexes. *Sci. Adv.* **7**, eabe5905 (2021).
56. M. Chiang *et al*., Bridging-induced phase separation and loop extrusion drive noise in chromatin transcription. arXiv [Preprint] (2024). http://arxiv.org/abs/2407.04907 (Accessed 13 July 2024).
57. G. Forte, L. Boteva, N. Gilbert, P. R. Cook, D. Marenduzzo, Bridging-mediated compaction of mitotic chromosomes. *Nucleus* **16**, 2497765 (2025).
58. G. Forte *et al*., Bridging condensins mediate compaction of mitotic chromosomes. *J. Cell Biol.* **223**, e202209113 (2023).
59. N. Naumova *et al*., Organization of the mitotic chromosome. *Science* **342**, 948–953 (2013).
60. F. Turci, N. B. Wilding, Phase separation and multibody effects in three-dimensional active Brownian particles. *Phys. Rev. Lett.* **126**, 038002 (2021).
61. T. A. de Pirey, F. van Wijland, Transitions driven by multibody interactions in an effective model of active matter. arXiv [Preprint] (2025). http://arxiv.org/abs/2510.18076 (Accessed 22 October 2025).
62. K. A. Dill, K. M. Fiebig, H. S. Chan, Cooperativity in protein-folding kinetics. *Proc. Natl. Acad. Sci. U.S.A.* **90**, 1942–1946 (1993).
63. M. P. Eastwood, P. G. Wolynes, Role of explicitly cooperative interactions in protein folding funnels: A simulation study. *J. Chem. Phys.* **114**, 4702–4716 (2001).
64. Y. Suzuki, J. N. Onuchic, Modeling the interplay between geometrical and energetic effects in protein folding. *J. Phys. Chem. B* **109**, 16503–16510 (2005).
65. V. G. Contessoto *et al*., Energy landscape analysis of the development of the chromosome structure across the cell cycle. *Proc. Natl. Acad. Sci. U.S.A.* **122**, e2425225122 (2025).
66. A. Goloborodko, M. V. Imakaev, J. F. Marko, L. Mirny, Compaction and segregation of sister chromatids via active loop extrusion. *eLife* **5**, e14864 (2016).
67. C. Hoencamp *et al*., 3d genomics across the tree of life reveals condensin II as a determinant of architecture type. *Science* **372**, 984–989 (2021).
68. T. Nozaki *et al*., Condensed but liquid-like domain organization of active chromatin regions in living human cells. *Sci. Adv.* **9**, eadf1488 (2023).
69. F. Conforto, Y. Gutierrez Fosado, D. Michieletto, Fluidification of entangled polymers by loop extrusion. *Phys. Rev. Res.* **6**, 033160 (2024).
70. F. Jülicher, J. Prost, Cooperative molecular motors. *Phys. Rev. Lett.* **75**, 2618 (1995).
71. S. Wang, P. G. Wolynes, On the spontaneous collective motion of active matter. *Proc. Natl. Acad. Sci. U.S.A.* **108**, 15184–15189 (2011).
72. P. Y. Plaçais, M. Balland, T. Guérin, J. F. Joanny, P. Martin, Spontaneous oscillations of a minimal actomyosin system under elastic loading. *Phys. Rev. Lett.* **103**, 158102 (2009).
73. F. C. MacKintosh, A. J. Levine, Nonequilibrium mechanics and dynamics of motor-activated gels. *Phys. Rev. Lett.* **100**, 018104 (2008).
74. S. Wang, P. G. Wolynes, Active contractility in actomyosin networks. *Proc. Natl. Acad. Sci. U.S.A.* **109**, 6446–6451 (2012).
75. T. L. Higashi, G. Pobegalov, M. Tang, M. I. Molodtsov, F. Uhlmann, A Brownian ratchet model for DNA loop extrusion by the cohesin complex. *eLife* **10**, e67530 (2021).
76. A. Bonato, C. A. Brackley, J. Johnson, D. Michieletto, D. Marenduzzo, Chromosome compaction and chromatin stiffness enhance diffusive loop extrusion by slip-link proteins. *Soft Matter* **16**, 2406–2414 (2020).
77. N. N. Bogoliubov, Kinetic equations. *J. Phys. USSR* **10**, 265–274 (1946).
78. M. Born, H. S. Green, A general kinetic theory of liquids I. The molecular distribution functions. *Proc. R. Soc. Lond. Ser. A. Math. Phys. Sci.* **188**, 10–18 (1946).
79. J. G. Kirkwood, The statistical mechanical theory of transport processes I. General theory. *J. Chem. Phys.* **14**, 180–201 (1946).
80. J. Yvon, Statistique des fluides et l'équation d'etat. *Actualits Sci. Indust.* **203**, 1–48 (1935).
81. Z. Cao, CaOaC/Processivity. GitHub. https://github.com/CaOaC/Processivity. Deposited 15 March 2026.
82. Z. Cao, C. Du, Z. Hou, P. G. Wolynes, Source code and data–theory of chromosome structural dynamics by processive loop extrusion. Zenodo. https://doi.org/10.5281/zenodo.20091942. Deposited 9 May 2026.

Downloaded from https://www.pnas.org by CAS University of Science and Technology of China USTC on May 29, 2026 from IP address 218.22.21.23.